Catalysis Today 180 (2012) 68–80

Contents lists available at SciVerse ScienceDirect

Catalysis Today

journal homepage: www.elsevier.com/locate/cattod

Structure sensitivity of the low-temperature water-gas shift reaction on Cu–CeO_2 catalysts

Rui Si[a], Joan Raitano[b], Nan Yi[a], Lihua Zhang[c], Siu-Wai Chan[b], Maria Flytzani-Stephanopoulos[a,*]

[a] Department of Chemical and Biological Engineering, Tufts University, Medford, MA 02155, United States
[b] Department of Materials Science, Columbia University, New York, NY 10027, United States
[c] Center for Functional Nanomaterials, Brookhaven National Laboratory, Upton, NY 11973, United States

ARTICLE INFO

Article history:
Received 24 December 2010
Received in revised form 25 August 2011
Accepted 11 September 2011
Available online 4 October 2011

Keywords:
Water-gas shift
Copper
Cerium oxide
Copper–ceria
Structure sensitivity
Shape effect

ABSTRACT

We have investigated the structure sensitivity of the water-gas shift (WGS) reaction on Cu–CeO_2 catalysts prepared at the nanoscale by different techniques. On the surface of ceria, different CuO_x structures exist. We show here that only the strongly bound Cu–[O_x]–Ce species, probably associated with the surface oxygen vacancies of ceria, are active for catalyzing the low-temperature WGS reaction. Weakly bound CuO_x clusters and CuO nanoparticles are spectator species in the reaction. Isolated Cu^{2+} ions doping the ceria surface are not active themselves, but they are important in that they create oxygen vacancies and can be used as a reservoir of copper to replenish surface Cu removed by leaching or sintering. Accordingly, synthesis techniques such as coprecipitation that allow for extensive solubility of Cu in ceria should be preferred over impregnation, deposition–precipitation, ion exchange or another two-step method whereby the copper precursor is added to already made ceria nanocrystals. For the synthesis of different structures, we have used two methods: a homogeneous coprecipitation (CP), involving hexamethylenetetramine as the precipitating agent and the pH buffer; and a deposition–precipitation (DP) technique. In the latter case, the ceria supports were first synthesized at the nanoscale with different shapes (rods, cubes) to investigate any potential shape effect on the reaction. Cu–CeO_2 catalysts with different copper contents up to *ca.* 20 at.% were prepared. An indirect shape effect of CeO_2, manifested by the propensity to form oxygen vacancies and strongly bind copper in the active form, was established; i.e. the water-gas shift reaction is not structure-sensitive. The apparent activation energy of the reaction on all samples was similar, 50 ± 10 kJ/mol, in a product-free (2% CO–10% H_2O) gas mixture.

1. Introduction

The water-gas shift (WGS) reaction ($CO + H_2O \leftrightarrow CO_2 + H_2$) plays an important role in fuel processing. For PEM fuel cell applications, novel low-temperature WGS catalysts are under development to upgrade the hydrogen-rich reformate gas streams where the catalyst possesses improved activity and greatly improved stability over the commercial Cu–ZnO catalysts [1,2]. The latter have been optimized for the production of chemicals, and are not suitable for fuel cell applications as they are pyrophoric and deactivate fast after exposure to air and/or water condensation. Because of its high activity [3] and low price, copper is still an excellent candidate as the active component of a new generation, stable catalyst for the WGS reaction. Many promising such catalyst compositions use cerium oxide (ceria, CeO_2) carriers, with the latter actively contributing to the making of an active and stable Cu-based catalyst.

As one of the most important rare earth oxides, ceria has been extensively applied in catalysis, electrochemistry, and optics, due to its unique physical and chemical properties. CeO_2 retains its defective fluorite-type crystal structure during the oxygen storage and release processes, and thus is an active oxide component of various oxidation catalysts used in diverse redox catalytic reactions [4,5]. Ceria-based catalysts are very good WGS catalysts [6–10], and the Cu–CeO_2 system was first reported by Li et al. as a promising low-temperature shift catalyst [7]. The choice of Cu–CeO_2 for high-temperature WGS applications was also rationalized [10], because this copper-based system is more stable than the commercial Cu/ZnO. For a practical fuel cell system, operating under frequent shutdown and restart cycles, ceria needs to be modified by addition of zirconia [11,12] or another dopant to avoid formation of Ce(III) hydroxycarbonate during shutdown to RT in the water-containing reaction gas. Another approach is to regenerate the catalyst frequently by oxidation at 400–450 °C [11–13] or to run the reaction in oxygen-assisted mode [13]. Despite this issue,

* Corresponding author. Tel.: +1 617 627 3048; fax: +1 617 627 3991.
E-mail address: maria.flytzani-stephanopoulos@tufts.edu
(M. Flytzani-Stephanopoulos).

0920-5861/$ – see front matter © 2011 Elsevier B.V. All rights reserved.
doi:10.1016/j.cattod.2011.09.008

ceria and doped ceria remains the support of choice when a highly dispersed metal preparation is desired, which must remain stable over a wide temperature range [10]; and when surface oxygen availability to the metal is required, as in the case of the water-gas shift reaction [9].

During the last decade, copper–ceria catalysts have been widely studied for the WGS reaction *via* different approaches. Synthesis, structural and surface investigations by multiple characterization techniques, activity and stability tests, investigations of the reaction mechanism, and determination of the active sites have been addressed. For example, Wang et al. observed reversible redox properties of copper in $Ce_{1-x}Cu_xO_2$ by *in situ* XAFS and time-resolved XRD measurements [14], and further found a complex interaction between copper and the oxygen vacancies of ceria [15]. Koryabkina et al. found that the addition of ceria did not increase the WGS rate per unit of Cu surface area, and claimed that ceria is not a promoter for copper [16], while Djinović et al. reported that the activity of CuO–CeO_2 catalysts for WGS reaction was related to the extent of surface CeO_2 reduction and the interaction between CuO and CeO_2 [17]. Thus, the basic questions regarding the structure–activity relationship and the interaction of copper and ceria in the WGS reaction have been addressed, but often with divergent conclusions. In our opinion, a consensus must be reached soon to enable better catalyst designs and development of active and stable water-gas shift catalysts for practical fuel cell applications. This will potentially lead to novel, properly designed Cu-containing CeO_2 catalysts of comparable activity to the more expensive choices of Pt- or Au-based WGS catalysts.

In this work, we have used different preparation methods to obtain the copper–ceria materials, developed a structural model for each sample, and attempted to correlate the catalyst activity to the presence or absence of certain Cu species and their interaction with the surface of ceria. The latter is an important ligand to the formation and stabilization of the active copper sites.

2. Experimental

2.1. Catalyst preparation

2.1.1. Synthesis of copper–ceria via coprecipitation (CP) method

$Ce(NO_3)_3{\cdot}6H_2O$ (99.5%, Alfa) and hexamethylenetetramine ($(CH_2)_6N_4$, > 99%, Alfa) were combined using a previously described procedure [18]. A solution of copper nitrate $Cu(NO_3)_2{\cdot}2.5H_2O$ (98.0–102.0%, Alfa), with a varying concentration to produce varying copper contents, was added to this reaction mixture under heating at 60–70 °C. The product was collected by filtration or centrifugation and then calcined in static air at 400 °C for 4 h.

2.1.2. Synthesis of copper–ceria via deposition–precipitation (DP) method

Rod- and cube-shaped CeO_2 supports were prepared *via* a controlled hydrolysis procedure, followed by a hydrothermal treatment [19]. The as calcined (air, 400 °C, 4 h) ceria nanopowders (3 g) were added in 150 mL DI water under stirring. $Cu(NO_3)_2{\cdot}2.5H_2O$ (3.08 mmol, 0.716 g) was dissolved in 75 mL DI water and added into the above CeO_2 solution dropwise. The pH was adjusted at 9 during the whole process by adding freshly made sodium carbonate (Na_2CO_3, 99.5%, Alfa) buffering solution (0.5 M) dropwise. The resulting precipitates were aged at room temperature for 1 h and then filtered, washed three times with DI water at room temperature. The product was dried in vacuum at 70–80 °C overnight, and then air-calcined at 400 °C for 4 h. In all air calcinations, the heating rate was 2 °C/min.

The samples reported here are denoted as *a*CuCe-*b*-(*L*), where *a* is the copper content in atomic percent ($a = [Cu/(Cu + Ce)]_{mol} \times 100$)], and *b* is the preparation method (CP: coprecipitation; Rod: deposition–precipitation on ceria nanorods; Cube: deposition–precipitation on ceria nanocubes). "*L*" stands for samples leached by sodium cyanide (NaCN) solutions [9]. The NaCN-leaching was done in a 2% NaCN–NaOH (pH = 12) aqueous solution at room temperature. An aqueous solution of ammonium carbonate ($(NH_4)_2CO_3$, 2 mol/L) was also used as leaching agent. The NaCN- or $(NH_4)_2CO_3$-leached samples were air-calcined at 400 °C for 4 h prior to testing. Hence, these samples were exposed at 400 °C for twice as long as the corresponding parent samples.

2.2. Characterization

The bulk metal composition in each sample was determined by inductively coupled plasma atomic emission spectrometry (ICP-AES, Perkin-Elmer, Plasma 40).

The BET specific surface area (*S*) was measured by single-point nitrogen adsorption/desorption measurements at 77 K in 30% N_2/He on a Micromeritics Pulse ChemiSorb 2705 instrument. The as-calcined samples were pretreated in He at 200 °C for 30 min.

The powder X-ray diffraction (XRD) patterns were recorded on a Rigaku RU300 X-ray generator with a 185 mm diffractometer (50 kV, 300 mA) or a Inel XRG 3000 diffractometer (30 kV, 30 mA), using Cu-Kα radiation (λ = 1.5406 Å). The scan was processed at a rate of 2°/min, and with a step of 0.02° for the former instrument. The lattice constant *a* of cubic Fluorite phase was calculated by least-squares refinement of cell dimensions from powder data, based on Cohen's Method [20,21]. The average grain size (*D*) was estimated according to the Scherrer equation [22], $D = 0.90\lambda/\beta\cos\theta$, where θ is the diffraction angle of the (1 1 1) peak of the cubic Fluorite phase, β is the full width at half maximum (FWHM) of the (1 1 1) peak (in radian), which is calibrated from high purity silica or bulk CeO_2 (5 μm) standard. The microstrain (ε) in the lattice of the as calcined crystallites was estimated by the single line method for analysis of XRD line broadening using a pseudo-Voigt profile function [23].

Transmission electron microscopy (TEM) was conducted on a JEOL 200cx instrument at 200 kV. The TEM samples were prepared by applying a drop of the ethanol suspension containing dispersed catalyst powders onto carbon-coated copper grids. High-resolution TEM (HRTEM) was done on a JEOL 3000F TEM/STEM (300 kV) at the Center for Functional Nanomaterials (CFN), Brookhaven National Laboratory (BNL).

The surface metal ratios of copper to cerium in the studied catalysts were determined by X-ray photoelectron spectroscopy (XPS) in an ion-pumped chamber of Axis Ultra (U.K.) spectrometer equipped with a focused mono-chromatic X-ray source (Al-Kα, $h\nu$ = 1486.6 eV). The sample powders were pressed on a copper electric tape for analysis. All the measurements were carried out at room temperature without any sample pre-treatment. The binding energy (*BE*) with a resolution of 0.1 eV was adjusted to the C 1s peaks at 285.0 eV.

The oxidation states of copper in each sample were identified by X-ray absorption near-edge structure (XANES) on the beamline X19A or X18B of National Synchrotron Light Source (NSLS) at BNL. Cu-K edge was investigated, and bulk CuO, Cu_2O and Cu were used as Cu^{2+}, Cu^{+}, and Cu^{0} standards, respectively. Experimental data were collected in the fluorescence mode with a PIPS detector. The X-ray absorption edge energy was calibrated by assigning the 8979 eV to the first inflection point in the standard Cu foil XANES. The *in situ* tests were carried out in a gas mixture of 5% CO/3% H_2O/He.

2.3. Catalytic tests

Temperature-programmed reduction by hydrogen (H_2-TPR) was carried out in a Micromeritics Pulse ChemiSorb 2705 instrument equipped with a thermal conductivity detector (TCD).

The catalyst powders were pre-oxidized in a 20% O_2/He gas mixture at 350 °C for 30 min, cooled down to room temperature and then purged with pure helium. The oxidized sample was heated from room temperature to 400 °C in a 20% H_2/N_2 gas mixture (20 mL/min) for H_2-TPR. The water produced during the test was frozen *via* an ice-water bath before TCD. Temperature-programmed reduction by carbon monoxide (CO-TPR) was carried out in 5% CO/He (60 mL/min) with 60–150 mg copper–ceria sample and monitored by mass spectrometry (MKS model RS-1). The first cycle was run under a heating rate of 5 °C/min without any pretreatment. After the measurement was finished, sample was cooled down to RT in pure helium flow. Then, the second cycle was run under the same heating rate without reoxidation treatment between the cycles. Similarly, temperature-programmed surface reaction by carbon monoxide plus water (CO + H_2O-TPSR) was carried out in 5% CO/3% H_2O/He.

Steady-state tests for the WGS reaction were conducted at atmospheric pressure over ~0.1 g powder samples diluted with silica sand (~0.2 g). Tests in both ascending and descending temperature modes (50 °C–step) were conducted to check for catalyst activation/deactivation. Data were collected after 1–2 h at steady-state. The gas mixture used in these tests was product-free, 2% CO/10% H_2O/He, and was flowed at 70 mL/min. A quartz tube (o.d. = 1 cm) with a porous quartz frit was used as a packed-bed flow reactor to support the catalyst. Water was injected into the flowing gas stream by a syringe pump. A condenser filled with ice was setup at the exit of the reactor to trap water. The feed and product gas streams were analyzed by a HP-6890 gas chromatograph (GC) equipped with a thermal conductivity detector (TCD). A 6 feet column was used to separate the gases.

Rate measurements were made in the same gas composition (2% CO/10% H_2O/He), but at much higher space velocities to ensure operation in the kinetic regime (<10–15% conversion of CO). CO and CO_2 concentrations in the outlet were continuously determined by a non-dispersive infrared (NDIR, IR-703) gas analyzer.

3. Results and discussion

3.1. Structure of Cu–CeO_2 catalysts prepared by coprecipitation (CuCe-CP)

The crystal phases of the 400 °C-calcined copper–ceria catalysts were identified by powder XRD. Fig. 1a shows that the Fluorite cubic CeO_2 (F_{m-3m}, JCPDS card: 34-394) is the only phase in the CuCe-CP samples. No peaks can be assigned to any of the copper species such as Cu, Cu_2O and CuO. HRTEM in Fig. 2a displays that the typical morphology of the copper–ceria nanocrystals is polyhedral. Again, no Cu/CuO_x lattice fringes were observed in the HRTEM images of different microdomains. Thus, either the formation of Cu–Ce–O solid solutions or ultra-fine CuO_x clusters are inferred for the CuCe-CP sample up to 19.6 at.% copper loading. It has been found that the solubility of copper in the CeO_2 lattice is strongly dependent upon the synthesis method and the post-treatment conditions (calcination temperature, time, etc.) [7,24,25]. Coprecipitation is by far the most effective way to prepare single-phase copper–ceria nanomaterials, and the isolated CuO_x phase was not observed by XRD up to 15 at.% Cu doping [24].

In the present work, hexamethylenetetramine, a mild base relative to more conventional ones for DP or CP (NaOH, $(NH_4)_2CO_3$, $NH_4{\cdot}H_2O$, etc.), was selected to precipitate cerium oxide crystallites and the metal precursor. The product was then crystallized fully into mixed oxides (CuO_x–CeO_2) during the calcination step.

To further investigate the structure of the **CuCe-CP** samples, the lattice constants of CeO_2 were calculated and are listed in Table 1 and Fig. 3. Fig. 3a shows that the lattice constant (a) of CeO_2 remains

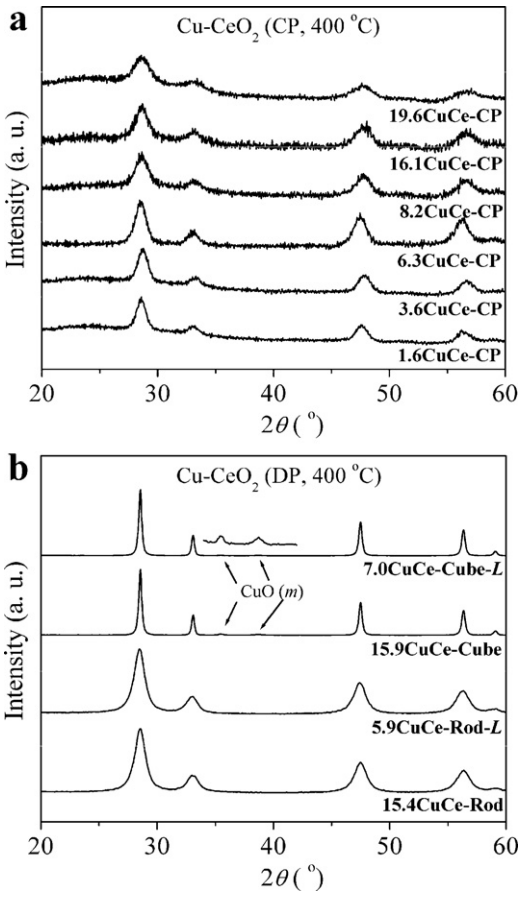

Fig. 1. XRD patterns of (a) CuCe-CP and (b) CuCe-DP.

unchanged with the increase of copper from 1.6 to 19.6 at.%. Similar results were previously reported by Wang et al. by using XRD with related density functional theory (DFT) calculations [14]. There are two different factors working on the a of ceria. The doping effect, i.e. substitution of a larger Ce^{4+} ion (97 pm, CN = 8) by a smaller Cu^{2+} ion (73 pm, CN = 6), contracts the CeO_2 cell. On the other hand, the formation of oxygen vacancies due to the aliovalent doping (Ce^{4+} by Cu^{2+}) or spontaneous creation of Ce^{3+} sites as the particle size of CeO_2 decreases has the opposite effect on the lattice constant of ceria [18,26,27]. From Fig. 3a, it is very clear that as the copper amount increases to *ca.* 20 at.%, the crystal size of CeO_2 calculated by the Scherrer equation decreases from 10 to 6 nm continuously. This is similar to the findings reported by Liu and Flytzani-Stephanopoulos, the increase of Cu concentration from 2 to 15 at.% resulted in the decrease of CeO_2 size from 10 to 7.6 nm [24]. Therefore, the combined effect caused by aliovalent doping and particle size keeps the lattice constants of CeO_2 unchanged throughout the whole copper concentration range examined.

Cyanide leaching was used to remove any weakly bound CuO_x clusters from the ceria surface/subsurface. Table 1 shows that the leachable copper content determined by the ICP-AES results increased with the Cu amount, i.e. from ~6% (1.6 at.% → 1.5 at.%) to 30% (19.6 at.% → 13.6 at.%). This indicates that most of copper species in the low Cu-content (1.6–6.3 at.%) samples are present as Cu^{2+} ions dopants in the ceria lattice or strongly interacting with the CeO_2 surfaces, while the fraction of weakly bound CuO_x clusters is non-negligible when the introduced copper exceeds the solubility limit of CuO in CeO_2 for the high copper-content (8.2–19.6 at.%) samples. Here, the definition of solubility limit is different from the conventional solid-state chemistry, i.e. that of a single phase after high-temperature (>1000 °C) sintering of the

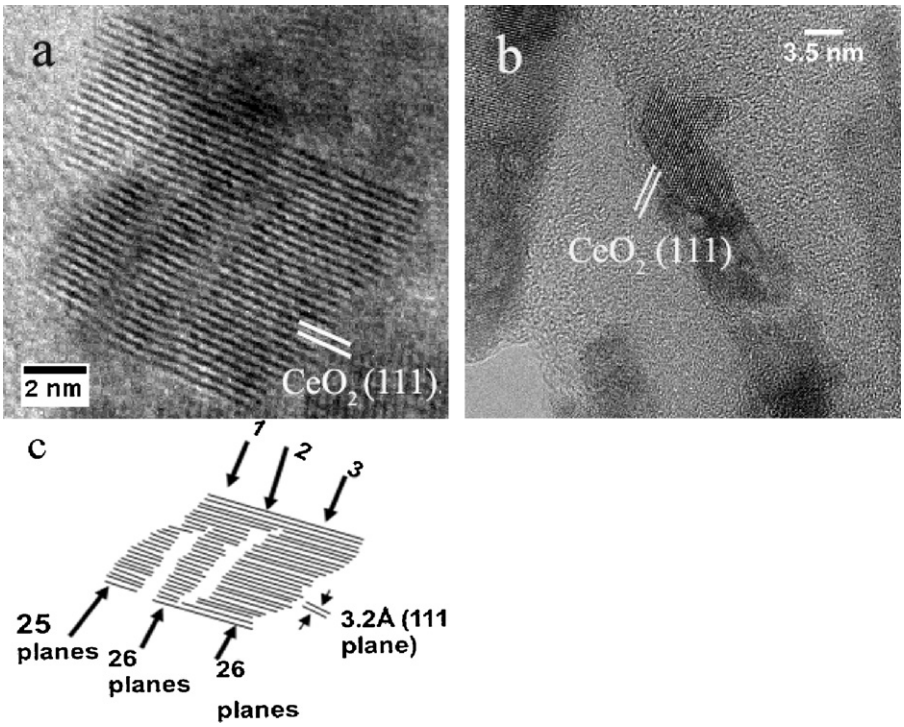

Fig. 2. HRTEM images of (a) 8.2CuCe-CP and (b) 15.4CuCe-Rod. (c) is the scheme of lattice dislocation in (a).

material. The surface of CuO/CeO_x was actually Cu-rich as the XPS data in Table 1 shows, but no segregated $Cu/Cu_2O/CuO$ phase was identified by XRD, indicating that the excess CuO_x species on the CeO_2 surface are either in amorphous form or too small to be detected. Wang et al. have reported a $Cu_{0.2}Ce_{0.8}O_x$ solid solution prepared by reverse microemulsion method and determined by time-resolved XRD [14]. The above ICP-AES data on both parent and leached copper–ceria catalysts also confirm the presence of weakly bound CuO_x species on the CeO_2 surface, which are "invisible" by typical XRD and TEM analyses [29]. These species were first reported by H_2-TPR on co-precipitated Cu–Ce–O_x materials by Liu and Flytzani-Stephanopoulos [24], and Kundakovic and Flytzani-Stephanopoulos [32]. Table 1 and Fig. 3 show that as the added Cu amount increases, the grain size of CeO_2 decreases, followed by a higher microstrain in the ceria lattice. The lattice strain, mainly caused by defects (point, step, plane, oxygen vacancy, etc.), is enhanced with high copper doping. These defects can be directly seen in the HRTEM images, e.g. as dislocations in Fig. 2a (see the scheme in Fig. 2c) and confirm the latter model to some extent.

On the basis of the above characterizations, the structures of CuCe-CP are described in Scheme 1a. Weakly bound copper oxide clusters, strongly interacting Cu–[O_x]–Ce surface species and Cu^{2+} ion dopants in the CeO_2 lattice coexist. Weakly bound CuO_x species are removed by sodium cyanide (pH = 12) at room temperature. These findings are further confirmed by the results of H_2-TPR characterization in the following.

Table 1 also shows that when the copper amount increases from 1.6 to 19.6 at.%, the BET specific surface area (S) of the CuCe-CP sample increases from 96 to 146 m^2/g, with a concomitant decrease of the grain size of CeO_2. In some previous reports, the S value dropped

Table 1
Bulk and surface analysis of the Cu–CeO_2 samples.[a]

Sample	Cu_{bulk} (at.%)	$Cu_{surf.}$ (at.%)	Phase	a (Å)	ε (%)	D (nm)	S (m^2/g)
1.6CuCe-CP	1.6(1.5)[b]	–	CeO_2 (c)	5.4115(6)[d]	1.7, 1.3, 1.2[e]	10.4	96
3.6CuCe-CP	3.6(3.2)	–		5.3863(5)	1.6, 1.6, 1.0	10.0	115
6.3CuCe-CP	6.3(3.6)	–		5.4131(2)	1.5, 0.8, 1.2	7.9	134
8.2CuCe-CP	8.2(6.0)	11.5, 17.8[c]		5.3980(7)	2.3, 1.8, 1.6	7.8	145
16.1CuCe-CP	16.1(10.8)	–		5.3981(7)	2.2, 2.0, 1.8	7.3	–
19.6CuCe-CP	19.6(13.6)	17.1, 18.7[c] (15.6[c])[b]		5.4036(4)	2.7, 2.7, 1.6	6.3	146
15.4CuCe-Rod	15.4	22.7		5.4149(1)	1.1, 1.1, 1.1	8.0	95
5.9CuCe-Rod-*L*	5.9	15.6		5.4150(1)	1.1, 1.1, 0.9	8.0	–
CeO_2-Rod	–	–		5.4118(1)	1.1, 1.3, 0.9	8.6	80
15.9CuCe-Cube	15.9	9.3	CeO_2 (c) + CuO (m)	5.4109(1)	0.4, 0.3, 0.2	34(17)[f]	29
7.0CuCe-Cube-*L*	7.0	–		5.4113(1)	0.4, 0.3, 0.2	34(13)	–
CeO_2-Cube	–	–	CeO_2 (c)	5.4060(1)	0.3, 0.2, 0.2	32	25

[a] a: lattice constants of CeO_2; ε: microstrain in CeO_2 lattice; D: grain size calculated from XRD; S: single-point BET specific surface area.
[b] Values in the brackets are for NaCN-leached samples.
[c] After the WGS reaction in 2% CO/10% H_2O/He up to 250 °C for *ca.* 15 h.
[d] Values in the brackets are errors for lattice constants a in 0.0001 Å.
[e] Calculated by single-peak method on CeO_2 (1 1 1), (2 0 0) and (2 2 0), respectively.
[f] Values in the brackets are for NaCN-leached samples.

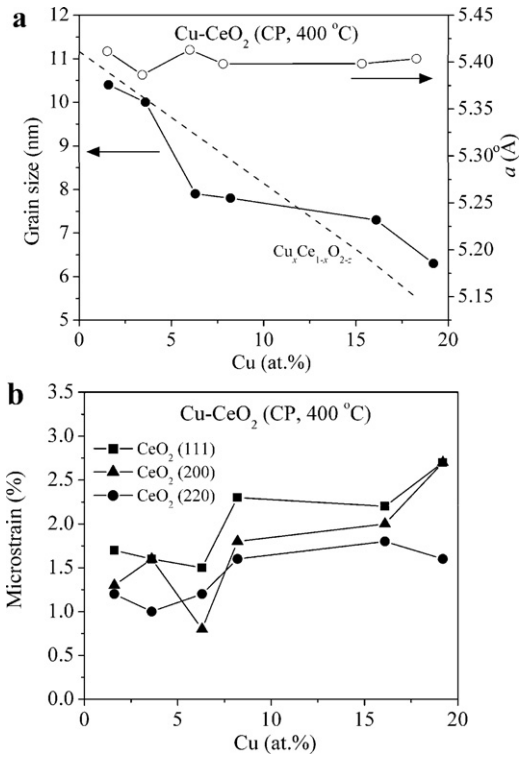

Fig. 3. (a) Grain size (solid) and lattice constants (open) of CuCe-CP as a function of Cu loading. Dash line is based on the theoretical calculation of a by using a_0 = 5.41134 Å (CeO_2, JCPDS card: 34-394), Ce^{4+} = 97 pm and Cu^{2+} = 73 pm; (b) microstrain in ceria of CuCe-CP as a function of Cu loading.

with increasing copper concentration for copper–ceria catalysts prepared by either incipient-wetness impregnation [6] or another coprecipitation method [28], while a trend similar to the one reported here was found in samples prepared by microemulsion-coprecipitation [29]. In this work, we attribute the increase in surface area with an increase in copper content to a more homogeneous coprecipitation of cerium and copper salts, which inhibits the segregated growth of the as-formed nuclei of ceria, and thus limits the grain growth of copper–ceria nanocrystals during the high temperature post-treatment, similar to what has been reported for the CeO_2–ZrO_2 system [30].

3.2. Structure of Cu–CeO_2 catalysts prepared by deposition–precipitation (CuCe-DP)

For comparison to the one-step coprecipitation route, we also examined a two-step approach whereby the Cu precursor was deposited onto the as-calcined nanoscale ceria supports by the DP. Instead of polycrystalline powders, single crystals of ceria were used with the ceria prepared as nanocubes and nanorods [19]. Table 1 shows that the structure (lattice constants and microstrain) and texture (grain size and surface area) of the CeO_2 crystals were unchanged after the corresponding copper deposition. Thus, the majority of the copper species are on the surface/subsurface of ceria, not doped into the bulk CeO_2 lattice.

From the XRD data of Fig. 1b, it can be seen that Cu–CeO_2-Rod is of pure Fluorite cubic CeO_2, while Cu–CeO_2-Cube contains a secondary phase of monoclinic CuO (Tenorite, $C_{2/c}$, JCPDS card: 41-254) with weak diffraction peaks at *ca.* 35.5° and 39.0°. HRTEM analyses also confirm the absence of Cu/CuO_x particles from the rod sample surface (Fig. 2b). In previous work, a strong shape effect of CeO_2 was found for the dispersion and hence the activity of gold species [19]. The ceria nanorods, enclosed by {1 1 0} and {1 0 0} planes, contain more surface oxygen vacancies than the ceria nanocubes, which expose {1 0 0} planes. Thus, gold ions/clusters were stabilized only on the CeO_2 nanorod surfaces, while Au nanoparticles were formed on the CeO_2 nanocubes [19]. Similarly, in the present work we find CuO_x clusters are highly dispersed on the ceria nanorods, while CuO particles were primarily formed on the {1 0 0} surfaces of the ceria nanocubes.

For these two types of Cu–CeO_2-DP catalysts, cyanide leaching was applied to distinguish different copper species on the CeO_2 supports. ICP-AES results demonstrate that the Cu concentrations in the rod and cube samples dropped from 15.4 and 15.9 at.% to 5.9 and 7.0 at.%, respectively (see Table 1). Around 60% of the total Cu in the parent catalysts was leached off. Due to the relatively lower cumulative formation equilibrium constants for copper-cyanide complex $[Cu(CN)_2]^-$ ($\log K$ = 24.0) [31] than that for $[Au(CN)_2]^-$ ($\log K$ = 38.3) [31], the cyanide leaching in copper–ceria system is not as powerful as that for the Au–CeO_2 catalysts used in a previous study [9]. Particularly, for the Cu–CeO_2-Cube, a small amount of copper oxide was identified by XRD, even after the room temperature leaching (see the enlarged pattern in Fig. 1b). The calculated grain size for copper oxide was reduced from 17 nm (parent) to 13 nm (leached). Thus, only the outmost layers of large CuO particles were leached by the above procedure. The inner core of the copper oxide nanocrystals, together with the strongly bound Cu–[O_x]–Ce species, were

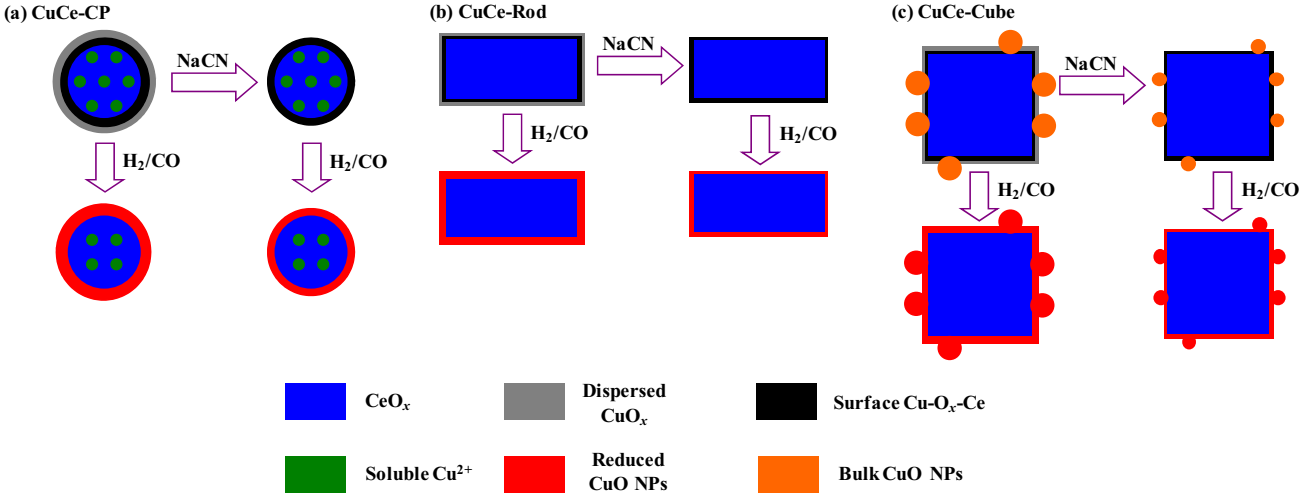

Scheme 1. Structures of (a) CuCe-CP, (b) CuCe-Rod, and (c) CuCe-Cube under different conditions (parent, leached, and H_2/CO reduced).

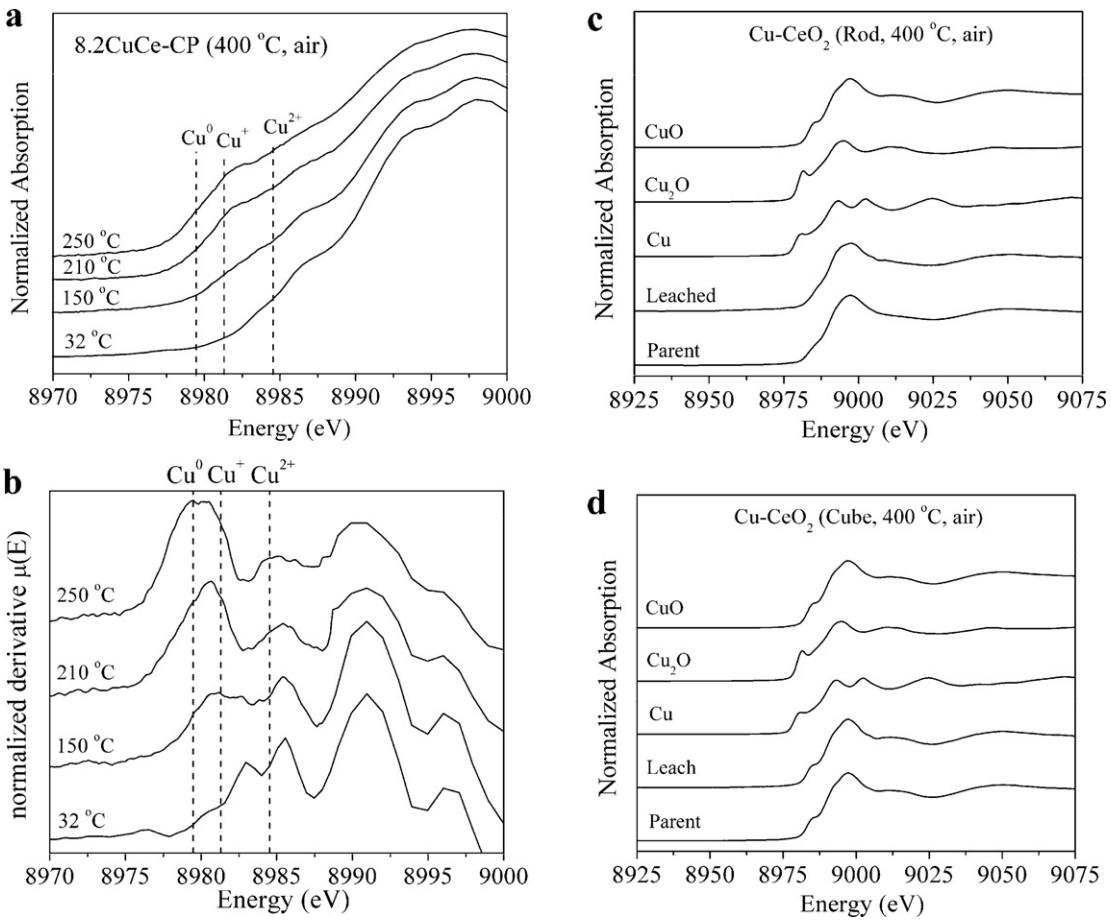

Fig. 4. Cu K-edge XANES profiles of (a) 8.2CuCe-CP (*in situ*, 5% CO/3% H_2O/He), (b) same as (a) derivative; (c) CuCe-Rod (ex-situ); and (d) CuCe-Cube (ex-situ).

preserved. For the Cu–CeO_2-Rod, both weakly bound (CuO_x clusters) and strongly bound Cu–[O_x]–Ce copper species were found by H_2-TPR on the CeO_2 surfaces after leaching.

Based on the above findings, the structure of CuCe-DP can be depicted as shown in Scheme 1. For the rod ceria sample, highly dispersed CuO_x clusters and strongly bound Cu–[O_x]–Ce species, and some CuO nanoparticles, are present (Scheme 1b). For the cube sample, bulk CuO nanoparticles dominate, but a small amount of strongly bound Cu–[O_x]–Ce copper species interacting with ceria are also present (see Scheme 1c). The identification of the type and amount of each Cu species will be detailed below in the TPR section.

3.3. Surface analysis of Cu–CeO_2 catalysts prepared by coprecipitation (CuCe-CP)

The surface Cu concentration was investigated by XPS. Table 1 shows an enrichment of copper (11.5 at.%) or a value very close to the bulk (17.1 at.%) for samples 8.2CuCe-CP and 19.6CuCe-CP, respectively. After the WGS reaction in the typical gas mixture of 2% CO/10% H_2O/He up to 250 °C, the surface copper content increased for both the parent (8.2CuCe-CP and 19.6CuCe-CP) and NaCN-leached (13.6CuCe-CP-*L*) samples. The final Cu concentration on the different surfaces of ceria was in the range of 15.6–18.7 at.%, regardless of the initial copper contents. This indicates that the lattice Cu^{2+} ion is not stable, and copper diffuses to the surface under the reaction conditions, the maximum amount of surface copper reaching a value of 15–20 at.%.

Due to the difficulty in distinguishing the $Cu^{2+}/Cu^{+}/Cu^{0}$ states by the XPS technique without including Auger peaks [24,27], XANES was used to determine the oxidation states of copper in the CuCe-CP samples. Fig. 4a and b show *in situ* XANES of the sample 8.2CuCe-CP using a CO-rich WGS reaction gas mixture (5% CO/3% H_2O/He). Cu^{2+}, was dominant at room-temperature, and was further reduced to Cu^{+} or Cu^{0} by CO at elevated temperatures (up to 250 °C). Thus, diffusion of lattice copper ions is followed by the surface reduction of Cu^{2+} under the WGS conditions. Similar results on the copper–ceria catalysts prepared by impregnation or reverse microemulsion have been reported by Wang et al. [15].

H_2-TPR was used to examine the reducibility of the studied copper–ceria catalysts, identifying the different surface oxygen species in each sample. Fig. 5 exhibits the H_2-TPR profiles for both the parent and leached copper–ceria catalysts. Compared with the pure CeO_2 support, which is normally reduced by H_2 above 350 °C (not shown), the addition of copper remarkably improves the reducibility of ceria [7,32], and the reduction of surface oxygen begins at 60–130 °C for the CP samples.

Fig. 5a and b show that the first reduction peak, located at 120–191 °C for the CuCe-CP samples (see Table 2), shifts with the amount of Cu on the surface and with the preparation conditions (e.g. before or after leaching). Correlating to the structure of the copper–ceria catalysts in Scheme 1a (refer to Section 3.1), this H_2-TPR peak is assigned to the reduction of highly dispersed CuO_x species, which includes small two- and three-dimensional clusters [32,33]. This weakly bound copper structure is easy to remove from the ceria support by NaCN-leaching for the low **Cu**-content samples (see Scheme 1b), but not from the high Cu samples (see dotted lines in Fig. 5b). An explanation for this is that the loss of weakly bound surface CuO_x species was compensated by diffusion of lattice Cu^{2+} ions to the CeO_2 surface [14] during the hydrogen heating step. The

Table 2
Reducibility and WGS activity of as prepared Cu–CeO_2 samples.

Sample	H_2-TPR		WGS reaction	
	H_2 consumption[a] (μmol/g)	Reduction T_{peak} (°C)	Rate[d] (μmol CO_2/g/s)	E_{app} (kJ/mol)
1.6CuCe-CP	183(115)[b], 177[c]	191, 245	0.25(0.0014)[e]	40.4 ± 3.2
1.5CuCe-CP-*L*	91(108), 91	291	0.37(0.0041)	50.4 ± 1.1
3.6CuCe-CP	1192(262), 842	177, 219, 294	0.57(0.0007)	50.4 ± 1.1
3.2CuCe-CP-*L*	645(232), 421	235, 372	0.46(0.0011)	52.6 ± 3.8
6.3CuCe-CP	1275(464), 258	173, 214, 236	1.7(0.0066)	60.8 ± 1.0
5.3CuCe-CP-*L*	792(389), 252	245, 358	0.69(0.0027)	45.1 ± 4.4
8.2CuCe-CP	1796(610), 603	126, 188, 200	3.0(0.0050)	44.5 ± 2.2
6.0CuCe-CP-*L*	1278(441), 679	145, 191	2.6(0.0038)	44.1 ± 2.4
16.1CuCe-CP	2390(1248), 700	137, 174, 197	2.8(0.0040)	50.4 ± 1.6
10.8CuCe-CP-*L*	1635(814), 826	136, 171, 199	1.5(0.0018)	34.2 ± 0.9
19.6CuCe-CP	2561(1547), 1378	120, 160, 186	1.9(0.0014)	52.1 ± 7.0
13.6CuCe-CP-*L*	1953(1040), 953	136, 163, 193	1.0(0.0011)	54.9 ± 6.3
15.4CuCe-Rod	1380(1189), 818	113, 146, 169	1.25(0.0015)	39.2 ± 2.1
5.9CuCe-Rod-*L*	1117(434), 939	173, 189	0.94(0.0010)	45.2 ± 1.8
15.9CuCe-Cube	1226(1231), 398	180, 211	0.51(0.0013)	45.5 ± 3.2
7.0CuCe-Cube-*L*	609(518), 338	201, 214	0.20(0.0006)	59.5 ± 1.6
10 at.% Cu–Ce(30% La)Ox	–	–	20 (250 °C)[f] 140 (350 °C)[f]	54[f]
8 wt.% Cu–CeO_2	–	–	0.11 (200 °C)[g]	56[g]
10 at.% Cu–CeO_2	–	–	–	47.5[h]
$Cu_{0.15}Ce_{0.85}O_x$	–	–	12 (200 °C)[i]	–
CuO–ZnO–Al_2O_3 (G66-A)	–	–	16 (200 °C)[i]	–

[a] Measured from room-temperature to 400 °C.
[b] Values in the brackets are calculated by assuming the complete reduction of CuO to Cu.
[c] Values after commas are attributed to strongly bound Cu–[O_x]–Ce (Peak B).
[d] Measured at 200 °C in 2% CO/10% H_2O/He.
[e] Values in the brackets are calculated TOF values (s^{-1}) by assuming all the active sites are from Peak B in H_2-TPR.
[f] Measured in 11% CO/23% H_2O/He, 250–450 °C [10].
[g] Measured in 7% CO/8.5% CO_2/22% H_2O/37% H_2/Ar [16].
[h] Measured in 12.9% CO/19.7% H_2O/12.2% CO_2/55.2% H_2 [28].
[i] Measured in 5% CO/He, H_2O/He pulse, GHSV = 26,300 h^{-1} [41].

reduction of this newly created copper oxide clusters exhibits the same profile as that of highly dispersed copper oxide species. This is plausible since the surface and bulk are in a dynamic equilibrium under the redox conditions applied. To prove this hypothesis, we compared the H_2-TPR profiles of both parent and leached CuCe-CP (high Cu) samples, and found that the intensity/area of reduction peak for Cu^{2+} in the CeO_2 matrix (Peak C in Fig. 5b, at 186–200 °C) is decreased drastically after the NaCN-leaching step. Restructuring of Cu–CeO_2 under the reducing conditions of H_2-TPR (20% H_2/N_2, 20 mL/min) takes place, and the Cu^{2+} ions in the ceria lattice are transformed to highly dispersed CuO_x clusters on the surface of CeO_2. This refilling of weakly bound CuO_x clusters by the lattice Cu^{2+} species was only observed on the catalysts with a high copper content (8.2–19.6 at.%), since the copper supply in the bulk of CeO_2 is depleted for the low Cu samples (see Fig. 5a). Diffusion of Cu^{2+} ions from the cerium oxide lattice to the CeO_2 surface and the subsequent reduction of ionic copper to metallic copper under certain reducing conditions has been reported by time-resolved XRD and *in situ* XANES/EXAFS of the Cu–CeO_2 system [14]. In general, a mixture of partially oxidized and metallic copper may be present under most conditions, especially since the Cu atoms at the interface with ceria can get oxidized by ceria: $Cu^0 + Ce^{4+} = Cu^+ + Ce^{3+}$. This has been reported even in H_2-rich environments for the copper–ceria system [34].

Higher temperature is required to reduce the copper in samples with very low copper concentration. For the 1.6CuCe-CP, the reduction peak is above the measurement limit (400 °C) and absent in Fig. 5a. Thus, this sample contains only lattice substituted copper ions, Cu^{2+}. Also, the leached 3.2CuCe-CP-*L* and 5.3CuCe-CP-*L* display higher reduction peak temperatures at 373 and 358 °C, respectively, than their parent materials (see Table 1); peaks assigned to "C".

The Peak "B" in H_2-TPR, is attributed to surface CuO_x species strongly interacting with ceria [35,36]. Fig. 5a and b show that Peak B shifts to lower values as the copper loading increases, e.g. from 245 °C in 1.6CuCe-CP to 160 °C in 19.6CuCe-CP (see also Table 2). This can be explained by the strength of the Cu–[O_x]–Ce interaction in each CuCe-CP sample, i.e. the number of Cu atoms clustered over an oxygen vacancy of ceria, and stabilized by the surrounding oxygen atoms of ceria. This argument is supported by comparing the H_2-TPR profiles of parent and leached copper–ceria. Fig. 5a shows that reduction occurs at higher temperatures for the CuCe-CP-*L* (Low Cu) samples. The applied NaCN–NaOH leaching effectively eliminated any weakly bound CuO_x from the parent catalysts. According to previous reports [7,17,36,37], the reduction peak of CuO_x clusters interacting with ceria in H_2-TPR varied from *ca.* 100 to 200 °C, depending upon multiple factors including copper concentration [10,17,36] and calcination temperature [17]. In this work, the reducibility of CeO_2 is determined by the strength of the Cu–[O_x]–Ce interaction at the boundary of the copper–ceria phases. Considering the big differences of the H_2-TPR profiles between low Cu (Fig. 5a) and high Cu (Fig. 5b) samples, we believe that there is a critical Cu concentration (6–8 at.%), below which most of the copper species reside in the bulk of CeO_2, instead of the surface sites.

The surface oxygen amounts of copper–ceria catalysts, determined by the hydrogen consumption in TPR tests, are listed in Table 2. Even if we assume that the surface oxygen originated from the complete reduction of Cu^{2+} to Cu^0 (upper limit), the experimental values greatly exceed the calculated ones (except for the 1.6CuCe-CP and 1.5CuCe-CP-*L* samples, in which reduction above 400 °C was not included experimentally), i.e. the O/Cu atomic ratio was higher than 1/1 (see Table 2). The actual O/Cu ratios are 1.7–4.5 for the parent CuCe-CP catalysts and 1.9–2.9 for the NaCN-leached ones. This confirms that doping of copper into the ceria support greatly promotes the reducibility of CeO_2 itself, and some of the surface (Peak B in H_2-TPR) and bulk (Peak C in H_2-TPR) Ce^{4+} ions can be reduced to Ce^{3+} at lower temperature than in pure ceria [7].

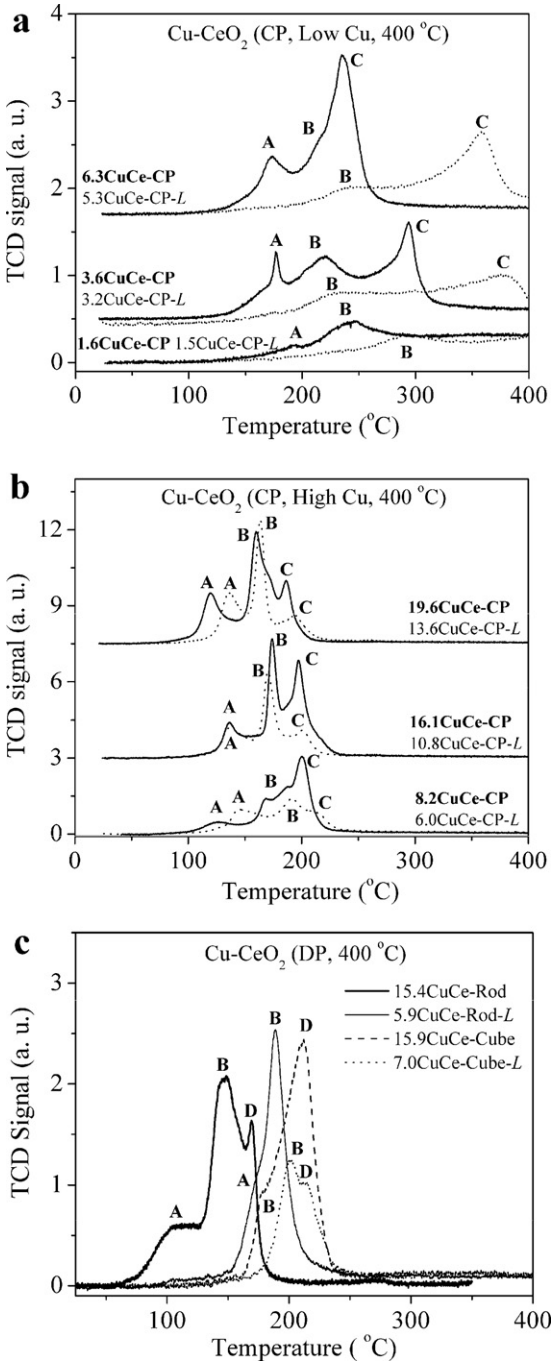

Fig. 5. H_2-TPR profiles of copper–ceria catalysts: (a) CuCe-CP (Low Cu); (b) CuCe-CP (High Cu); (c) CuCe-DP. Labels represent the reduction of (A) highly dispersed CuO_x clusters, (B) Cu–[O_x]–Ce, (C) Cu^{2+} ion in CeO_2 lattice, and (D) bulk CuO particles.

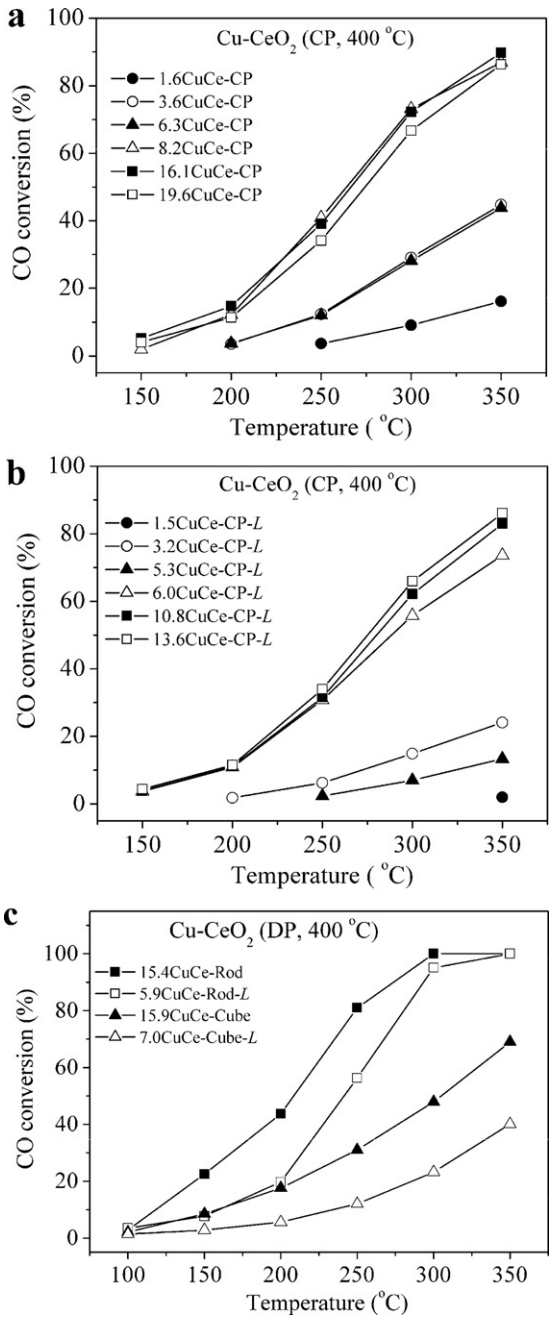

Fig. 6. Steady-state conversion profiles over copper–ceria catalysts in the WGS reaction (2% CO/10% H_2O/He): (a) CuCe-CP; (b) CuCe-CP-*L*; (c) CuCe-DP.

3.4. Surface analysis of Cu–CeO_2 catalysts prepared by deposition–precipitation (CuCe-DP)

According to the XPS data shown in Table 1, copper was highly enriched on the surface of CuCe-Rod with a surface concentration of 22.7 and 15.6 at.% for the parent (15.6CuCe-Rod) and leached (5.9CuCe-Rod-*L*) samples, respectively. This is consistent with the XRD results, i.e. Cu mainly exists on the surface or subsurface of CeO_2 prepared by the two-step deposition–precipitation method. However, for the fresh CuCe-Cube sample, the surface copper was 9.3 at.%, much less than the value of 15.9 at.% measured by ICP. This can be explained by the formation of large-sized CuO particles (17 nm of average dia. according to XRD), larger than the mean escape depth (~1.2 nm, calculated from Tanuma, Powell, and Penn TPP2M formula [38]) of the generated photoelectrons. Thus, the XPS underestimates the amount of surface Cu in this case. Cu^{2+} was the only chemical species determined by the Cu K-edge XANES analysis in the as calcined CuCe-Rod (parent and leached, Fig. 4c) and CuCe-Cube (parent and leached, Fig. 4d) samples.

The H_2-TPR profiles of the copper–ceria catalysts prepared by the DP method are shown in Fig. 5c. For sample 15.4CuCe-Rod, a wide band starting from *ca.* 60 °C, a strong peak centered at 146 °C and a sharp reduction around 169 °C are observed. The first one is attributed to the reduction of highly dispersed copper oxide species [32,33], the next one to the reduction of CuO_x clusters interacting with ceria at different strengths [35,36], and the last one is due to the reduction of CuO nanoparticles on the surface of CeO_2.

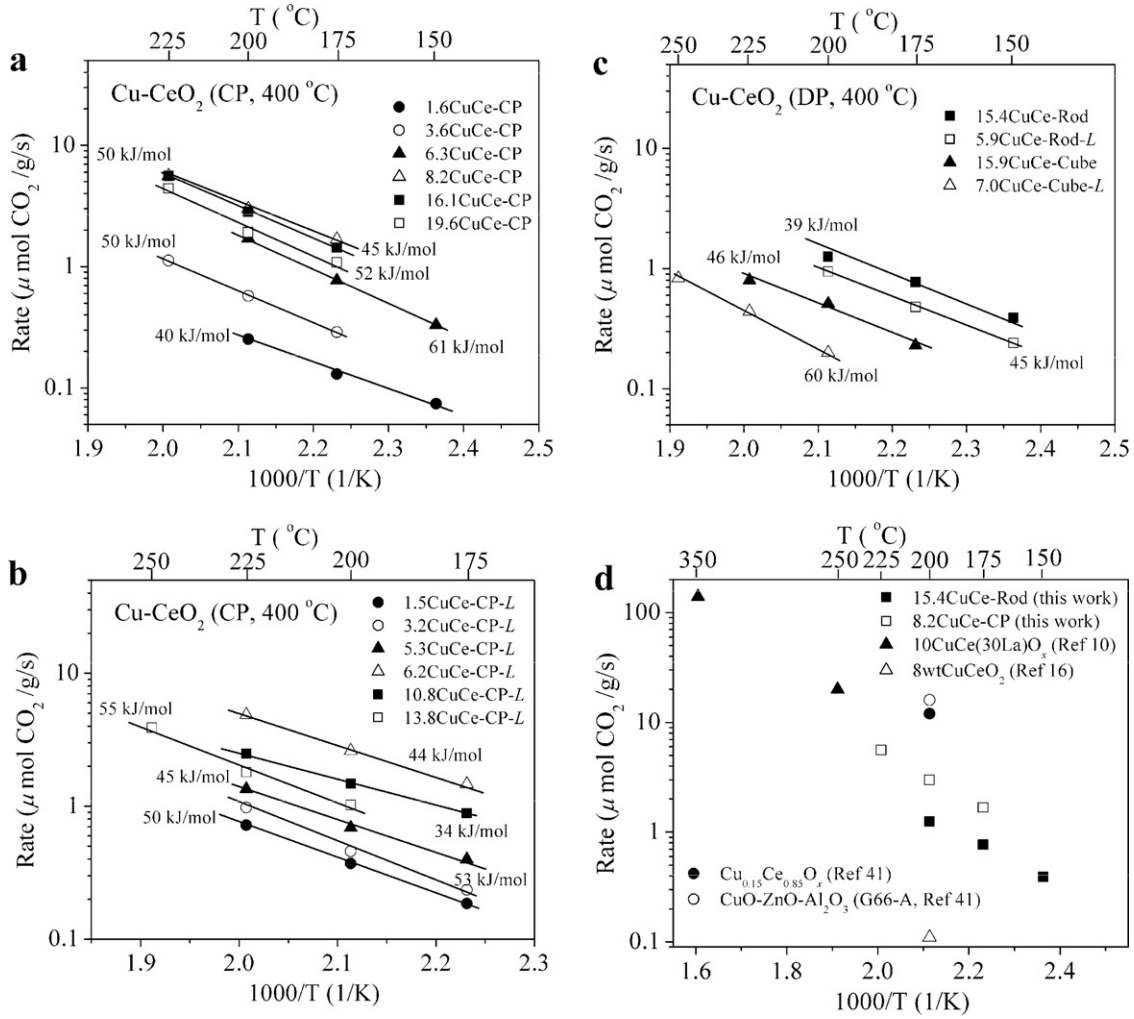

Fig. 7. Reaction rates (2% CO 10% H_2O/He) of copper–ceria catalysts for the WGS reaction: (a) CuCe-CP; (b) CuCe-CP-*L*; (c) CuCe-DP; (d) comparison with other reports.

The isolated CuO particles were "invisible" by XRD, probably due to CuO concentration below the detection limit of the X-ray technique (~2 wt.%). Cu^{2+} ions in the CeO_2 lattice are absent from the ceria nanorod sample, in good agreement with the structural model in Scheme 1b. After NaCN-leaching, TPR of 5.9CuCe-Rod-*L* shows a strong peak at 189 °C, assigned to the reduction of strongly bound CuO_x clusters with a higher reduction temperature than the parent. The O/Cu ratio, based on the experimental and theoretical (for complete reduction of CuO to Cu) values of H_2-consumption, distinctly increased from 1.2 (parent) to 2.6 (leached).

For sample 15.9CuCe-Cube, Fig. 5c exhibits a single H_2-TPR peak located at 211 °C. The peak position was unchanged after the NaCN-leaching, but the intensity greatly decreased (see dotted line in Fig. 5c). Correlating to the structure demonstrated in Scheme 1d, this peak is due to the reduction of bulk CuO particles, which typically appears around 200 °C in H_2-TPR [7]. There is also a shoulder at *ca.* 180 °C on the H_2-TPR of the parent 15.9CuCe-Cube, which was intensified to a sharp peak at the higher temperature of 201 °C in the leached 7.0CuCe-Cube-*L*. This is generated by the reduction of strongly bound Cu_nO clusters interacting with the ceria support [35,36]. The O/Cu ratio of copper on ceria nanocubes increased from 1.0 (parent) to 1.2 (leached) because of lower abundance of the CuO nanoparticles in the leached sample; Peak B/Peak D ratio increases in the leached sample. Overall, less of the surface oxygen of ceria is reduced here, the reason being the fewer sites of ceria-bound copper on the {1 0 0} surfaces of the ceria cubes. In turn, this is attributed to the small number of oxygen vacancies on the ceria cubes because of their large size (30 ± 11 nm). Thus, Cu cannot disperse well on the nanocubes. Similar observations were made for the dispersion of Au on CeO_2 nanoshapes [19].

3.5. WGS activity

Figs. 6 and 7 exhibit the steady-state conversion of CO and the Arrhenius-type plots for the WGS reaction rates over the various copper–ceria catalysts considered here. Three characteristics have been observed for the coprecipitation samples. First, the CO conversion increased with the copper amount and reached a maximum at 8.2 at.% Cu. The CO conversion remained the same or dropped a little for samples with higher copper contents. This is corroborated by the rate measurements under the same reaction conditions (see Fig. 7a and b and Table 2). Among the samples, 8.2CuCe-CP and its leached derivative, 6.0CuCe-CP-*L*, shows the highest reaction rate (3.0 and 2.6 μmol CO_2/g/s, respectively) at 200 °C. Second, the activity of NaCN-leached copper–ceria catalysts for the WGS reaction was slightly lower than that of the parent materials (before scaling by the surface copper amount). Again, the reaction rates showed the same trend. Third, despite the big difference of the WGS reaction rates over the CuCe-CP catalysts, the corresponding apparent activation energies from the Arrhenius plots were similar, in the range of 40–60 kJ/mol. This suggests that the reaction mechanism is the same, the only difference being the number of active sites, which varied with the Cu content and reached a maximum at ~8 at.% Cu. Also, the apparent activation energy calculated in this work

(40–60 kJ/mol) is consistent with previously reported values on copper–ceria catalysts measured under different gas compositions, e.g. for 8 at.% Cu–CeO_2 (56 kJ/mol) by Koryabkina et al. [16], 10 at.% Cu–Ce(30% La)O_x (54 kJ/mol) by Qi and Flytzani-Stephanopoulos [10], 4–10 at.% Cu–CeO_2 (45–54 kJ/mol) by Zerva and Philippopoulos [28], and $Cu_{0.1}Ce_{0.9}O_{2-y}$ (51 kJ/mol) by Kušar et al. [39].

For the Cu–CeO_2 catalysts prepared by the DP method, the WGS reaction rates decreased in the order 15.4CuCe-Rod > 5.9CuCe-Rod-*L* > 15.9CuCe-Cube > 7.0CuCe-Cube-*L*, as can be seen by the CO conversion profiles of Fig. 6c, the Arrhenius-type plots in Fig. 7c, and the reaction rates listed in Table 2. This shape effect of CeO_2 is similar to our recent report on Au–CeO_2 WGS catalysts [19]. However, with the latter, the leached catalysts had the same activity as the parent, indicating that cyanide-leaching removes some of the active sites in the case of the Cu–CeO_2 catalysts. We also tested the activity of Cu-free CeO_2 nanorods and nanocubes. No CO_2 product was detected up to 400 °C on either support. So, even in the least active catalyst (7.0CuCe-Cube-*L*), there is some interaction of Cu and CeO_2 support as seen by the incomplete leaching of CuO particles confirmed by XRD, and the consumption of H_2 in TPR, Fig. 5c. This explains why the observed activity for the leached Cu/ceriacube sample exceeds that of the Cu-free ceria nanocubes.

Similar to the case of Au/CeO_2 nanoshapes, the shape effect on the WGS reactivity of CuO_x is indirect; i.e. it is manifested through the dispersibility of Cu on the various surfaces. The ceria nanocube (30 nm) is larger than the nanorods (10 × 50–150 nm) and composed of {1 0 0} planes, hence more difficult to form oxygen vacancies than the nanorod {1 1 0} surfaces [40], the latter containing more anchoring points for the CuO_x species than the former.

The reaction rates in this work were consistent with our previous results on the Cu–CeO_2 catalysts for high-temperature (250–450 °C) WGS reaction, although the water concentration was higher in the latter (11% CO/23% H_2O/He). Fig. 7d exhibits that the reported rates (8.2CuCe-CP, 15.4CuCe-Rod in this work; and 10 at.% Cu–Ce(30% La)O_x [10]) are similar and the high-temperature data lie on the extension of low-temperature ones. No change of mechanism with temperature is concluded from these results. Due to the different preparation methods (DP, CP, and impregnation) and testing conditions (gas composition, pretreatment), the rates over our copper–ceria catalysts and those reported by other groups [16,41] show some variability (see Table 2 and Fig. 7d).

On the basis of the above findings, we can correlate the WGS activity with one of the identified CuO_x species on the ceria surfaces. These species are: (1) the weakly bound CuO_x species (Peak A in H_2-TPR). This may be a cluster of Cu atoms stabilized over adsorbed oxygen species, such as superoxide, on ceria, e.g. $(Cu_n)^{\delta+}$–O–O–Ce–(n = 2–6). Stable superoxide on ceria up to 873 K has been found by ESR spectroscopy [42]; (2) single or multiple Cu atom cluster, Cu–[O_x]–Ce, stabilized over an oxygen vacancy of ceria (Peak B in H_2-TPR); (3) lattice substituting Cu^{2+} ion (Peak C in H_2-TPR); (4) CuO nanoparticles displaying bulk CuO properties on the ceria surface.

In this work, the WGS reaction activity of the different copper–ceria catalysts is found to be a function of the synthesis method and copper loading. The reason these are important parameters is probably that they can control the structure of the surface and the concentration of the active species which in turn controls the activity. According to the *in situ* XANES data presented here in Fig. 4, as well as previous reports using *in situ* XRD and EXAFS [14,15,43], only oxidized copper species are present in the fresh copper–ceria catalyst, and the creation of metallic copper (Cu^0) is dependent upon the chemical potential of the reducing gases used and the reaction temperature applied. The active sites are stabilized by ceria; hence the support may be viewed as a ligand for the cluster, preserving its partially oxidized state. In experiments where we intentionally pre-reduced the 15.4CuCe-Rod sample in 20% H_2/He at 250 °C for 1 h, the initial activity dropped – e.g. the 200 °C-reaction rate from 1.25 (fresh) to 0.50 μmol CO_2/g/s (pre-reduced).

Recently, Barrio et al. [44] emphasized the importance of the interaction between copper and ceria in their inverse CeO_2/CuO structured catalysts for the WGS reaction. The interaction with ceria is important to keep the CuO_x species dispersed, and we think this means to preserve the Cu in a partially oxidized state. While the attribution of activity to Cu^0 alone is often a conclusion from XANES and other experiments [15], it should be noted that the active sites may be the minority species, hence very hard to detect/count with these techniques. The fact that extension of the application of Cu–CeO_2 to high-temperature WGS can be made, Fig. 7d, without a change in the apparent activation energy [10], argues in favor of the same mechanism operating throughout the temperature range from 100 to 350 °C.

To further investigate the reactivity and relevance of the different CuO_x species on ceria, we conducted a series of CO-TPR tests. Unlike H_2-TPR, which determines the type and amounts of all reducible surface oxygen species, CO-TPR can pinpoint the onset of the activation of surface – OH groups, i.e. the lightoff temperature of the WGS reaction at which both CO_2 and H_2 are produced together. Fig. 8a and b show cyclic CO-TPR profiles of 15.4CuCe-Rod sample. For the first cycle, weakly bound CuO_x species (Peak A in H_2-TPR), strongly bound Cu–[O_x]–Ce species (Peak B in H_2-TPR), and CuO nanoparticles (Peak D in H_2-TPR) were determined from the CO_2 signal (m/z = 44) at 60–140 °C, 200–250 °C, and 160–190 °C, respectively. Compared with the H_2-TPR results, the reduction of isolated CuO nanoparticles was shifted to a lower temperature in CO-TPR, lower than the reduction temperature of strongly bound Cu–[O_x]–Ce species. This is due to the different responses of CuO nanoparticles to the probe molecules (H_2 and CO). To further prove the above assignment, $(NH_4)_2CO_3$-leaching was carried out on the 15.4CuCeRod and 15.9CuCeCube catalyst. Fig. 9a and c show that the CO-reduction was shifted to higher temperatures for the $(NH_4)_2CO_3$-leached samples (starting from 150 °C), compared with those for the NaCN-leached (starting from 60 °C), since ammonium carbonate is more strongly bound to copper ion than the cyanide ligand. More importantly, it can be clearly seen that the second CO-TPR peak in $(NH_4)_2CO_3$-leached CuCe samples (Fig. 9a and c) was much weaker than that on the NaCN-leached ones (Fig. 8a and c). This is due to the more effective leaching of CuO particles by $(NH_4)_2CO_3$ [46], directly supporting that that the sequence of Peaks A, B, D/C changes with different reducing agents, i.e. H_2 (Fig. 5) and CO (Figs. 8 and 9), No hydrogen was generated from the reduction of weakly bound CuO_x clusters or isolated CuO particles. The onset of the WGS reaction was around 180 °C, accompanied by the reduction of strongly bound Cu–[O_x]–Ce species. This indicates that the active sites on Cu–CeO_2 catalysts are the Cu–[O_x]–Ce species (Peak B in H_2-TPR), which is further corroborated by the second cycle of CO-TPR. Fig. 8b exhibits the same H_2 onset and profile up to 400 °C as that of the first cycle (Fig. 8a), revealing that activated surface hydroxyls were not fully depleted in the first cycle. However, no CO_2 peak at 160–190 °C was found, i.e. the adsorbed oxygen on CuO nanoparticles was totally consumed during the first cycle. H_2 production paralleled the CO_2 production from the WGS reaction activated by the strongly bound Cu–[O_x]–Ce species at 170–270 °C. Again, for the $(NH_4)_2CO_3$ – leached rod and cube samples, we observed that Peaks A and D in CO-TPR (Fig. 9a and c) were not involved in CO + H_2O-TPSR (Fig. 9b and d). The release of a significant amount of hydrogen was a result of activation of –OH by CO adsorbed on the Cu–[O_x]–Ce species. Thus, these species are the active sites for the WGS reaction. We further checked the Cu–CeO_2 catalysts made by other preparation methods (CP, DP on ceria nanocubes), and found the same CO-TPR results (see Fig. 8c and d), except that the sharp

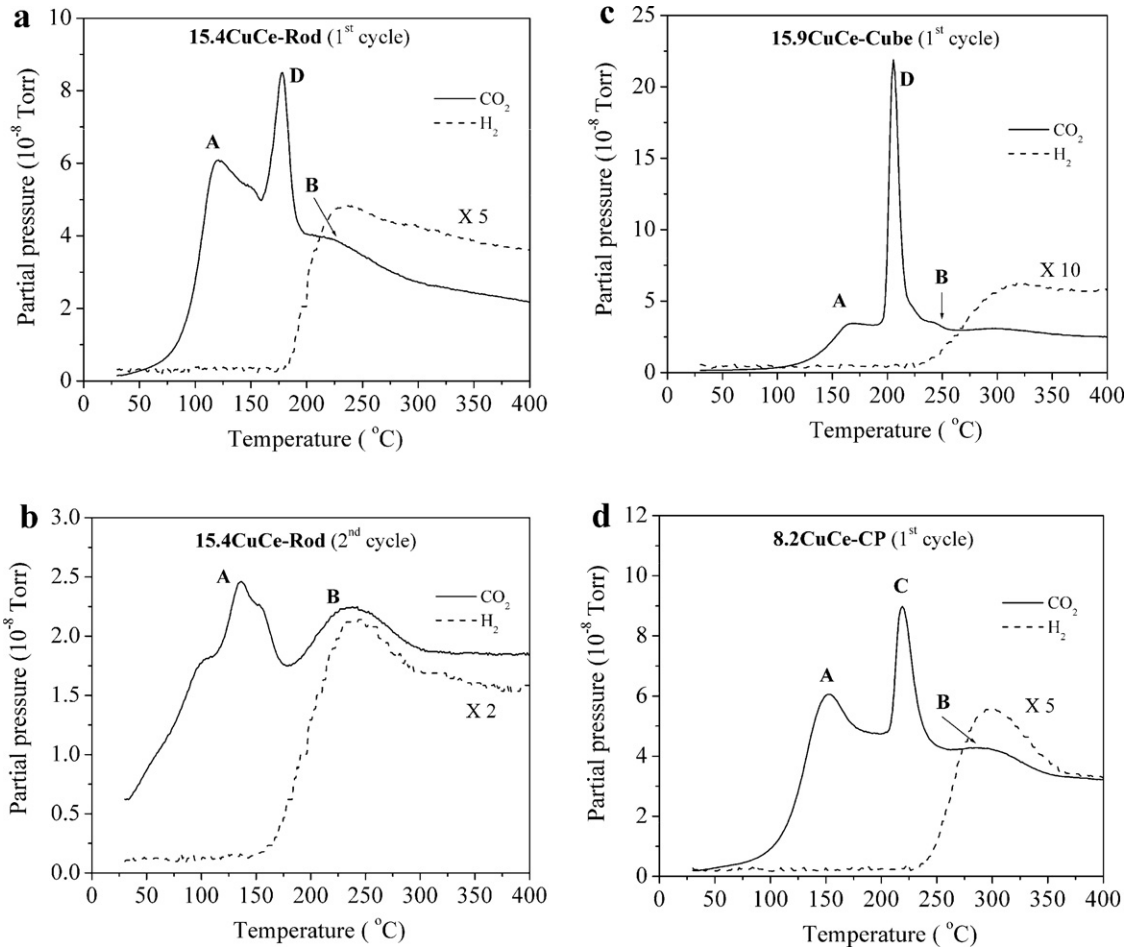

Fig. 8. CO-TPR profiles of (a) 15.4CuCe-Rod. 150 mg, 1st cycle; (b) 15.4CuCe-Rod. 150 mg, 2nd cycle; (c) 15.9CuCe-Cube 60 mg; (d) 8.2CuCe-CP. 60 mg. No pretreatment before each cycle. Labels represent the reduction of (A) highly dispersed CuO_x clusters, (B) Cu–[O_x]–Ce, (C) Cu^{2+} ion in CeO_2 lattice, and (D) bulk CuO particles.

CO_2 peak around 200–250 °C was assigned to the reduction of Cu^{2+} ions in the ceria lattice (Peak C in H_2-TPR).

Based on the present experimental data (ICP-AES, XRD, XPS, XANES, H_2- and CO-TPR and the activity tests) we can advance the following assessment of the active sites of a Cu–CeO_x catalyst for the WGS reaction:

(1) Highly dispersed CuO_x species on ceria (grey in Scheme 1 and Peak A in H_2-TPR) are not the active species for the low-temperature water-gas shift reaction. Although providing stable surface oxygen at low temperatures around 100 °C in both H_2-TPR and CO-TPR, this species could not activate the WGS reaction and no hydrogen accompanied the CO_2 production at this temperature window (see CO-TPR in Fig. 8). This species is of course a powerful dry CO oxidation catalyst.

(2) Strongly bound Cu–[O_x]–Ce species (black in Scheme 1 and Peak B in H_2-TPR) are active sites for low-temperature (<350 °C) WGS reaction on copper–ceria catalysts. CO-TPR clearly reveals that CO adsorbed on this species activated the –OH groups at the site and H_2 was produced (see Fig. 8). Previously, it has been shown that CeO_2 is not a simple spectator in the WGS reaction with copper–ceria catalysts [10,16,17,45]. In this paper, we have tried to distinguish the Cu–O–Ce interactions by carefully selecting different preparation methods and copper concentrations (see Scheme 1), and found that the activity of copper–ceria catalysts for the WGS reaction is due solely to the strongly bound Cu–[O_x]–Ce species with an apparent activation energy is 50 ± 10 kJ/mol.

(3) Cu^{2+} ion dopants in the ceria lattice (green in Scheme 1a and Peak C in H_2-TPR) are inactive, but serve as a copper reservoir and supply fresh active copper sites upon reduction and during reaction. For the CuCe-CP catalysts, the highly dispersed copper oxide species (grey in Scheme 1a) are washed away by sodium cyanide, but are replenished by diffusion of the Cu^{2+} ions from the bulk CeO_2 lattice to the surface during the WGS reaction (2% CO/10% H_2O/He) if the concentration of copper is high enough. By XPS, we identified that surface copper was increased for the used NaCN-leached sample, compared with the fresh leached one, confirming the diffusion of lattice Cu^{2+} ions during the WGS reaction. In CO-TPR (see Fig. 8d), the reduction of Cu^{2+} ions in the ceria lattice was not accompanied by the generation of H_2, further confirming that this species is not the active site for the WGS reaction. Similar results for oxide solid solutions of copper and cerium have been reported previously. Wang et al. found that a 5 wt.% Cu/CeO_2 prepared by impregnation (copper-on-ceria) shows higher activity for the WGS reaction than the $Ce_{0.8}Cu_{0.2}O_2$ solid solution prepared by reverse microemulsion method (copper-in-ceria) [15].

(4) CuO particles (orange in Scheme 1 and Peak D in H_2-TPR) are inactive. For the CuCe-DP catalysts, the ceria cube samples were much less active for the WGS reaction than the rod samples, even though they both contained a similar concentration of Cu (Fig. 6c and Table 2). Large (17 nm-dia.) CuO nanocrystals were confirmed as the major fraction of Cu in these catalysts. Also, the CO-TPR results (Fig. 8c) prove that the isolated CuO particles are inactive during the WGS reaction.

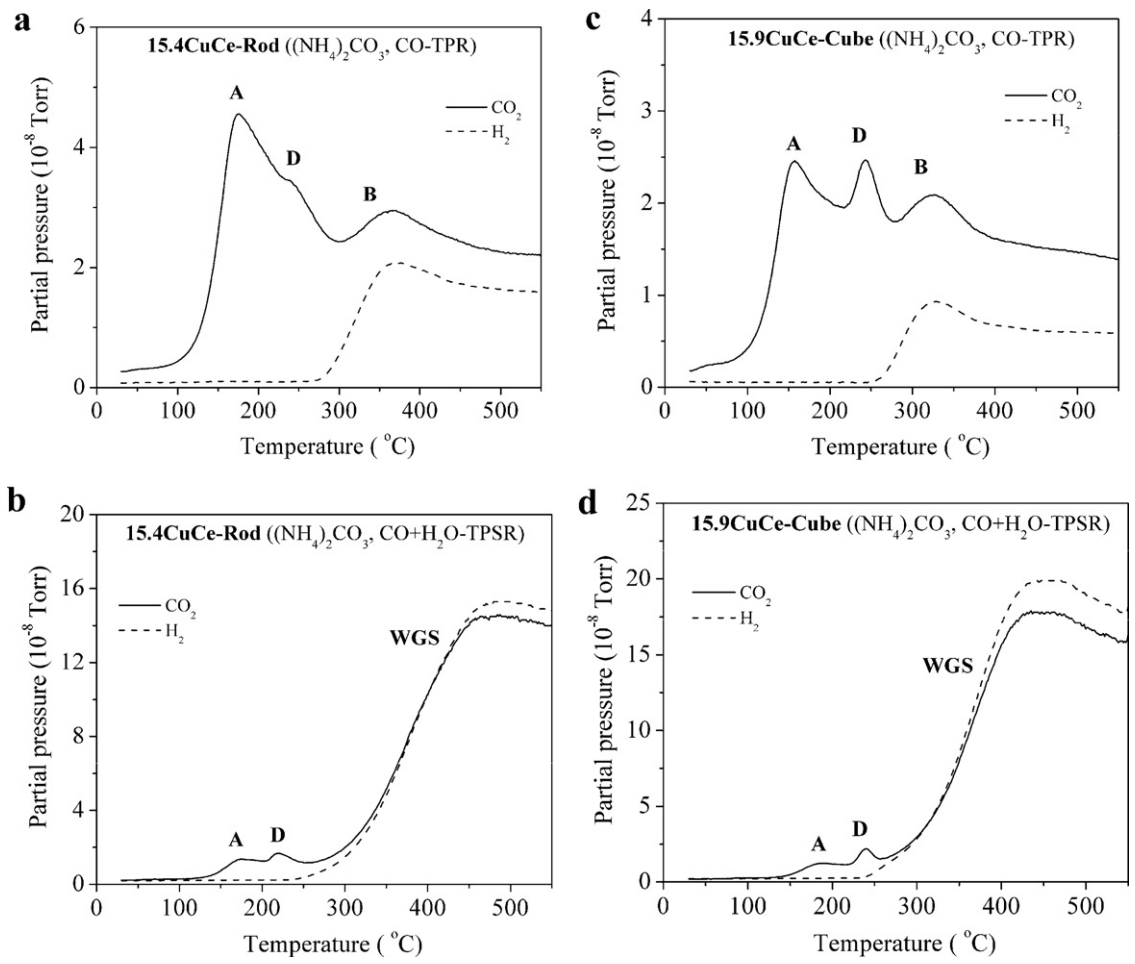

Fig. 9. CO-TPR profiles of (a) 15.4CuCe-Rod leached by $(NH_4)_2CO_3$; (c) 15.9CuCe-Cube leached by $(NH_4)_2CO_3$ and CO + H_2O-TPSR profiles of (b) 15.4CuCe-Rod leached by $(NH_4)_2CO_3$; (d) 15.9CuCe-Cube leached by $(NH_4)_2CO_3$. Labels represent the reduction of (A) highly dispersed CuO_x clusters, (B) Cu–[O_x]–Ce, and (D) bulk CuO particles.

4. Conclusions

In this work, we have used two preparation methods, coprecipitation and deposition–precipitation to obtain Cu–CeO_2 catalysts with four different copper–ceria structures, i.e. highly dispersed or weakly bound CuO_x clusters, copper oxide species strongly interacting with ceria (Cu–[O_x]–Ce), Cu^{2+} ions in the CeO_2 lattice, and CuO nanoparticles. The activity tests and the related characterizations (ICP-AES, HREM, XPS, XRD, H_2-TPR, and CO-TPR) have identified that only the strongly bound Cu–[O_x]–Ce species are the active sites for the low-temperature WGS reaction. An indirect shape effect of CeO_2, manifested by the propensity to form oxygen vacancies and strongly stabilize copper in the active form, was observed. The apparent activation energy of the reaction on all samples was similar, 50 ± 10 kJ/mol, implying that the WGS reaction on these catalysts followed the same reaction mechanism. Thus, the water-gas shift reaction for copper on different CeO_2 nanoshapes is not structure-sensitive. In selecting the proper catalyst amounts and methods of preparation, the findings of this work rationalize the design of ~10–15 at.% Cu in nanoscale ceria prepared by a single-step coprecipitation method in order to maximize the concentration of active sites B (Cu–[O_x]–Ce) after calcination in air to 400 °C. If a DP or impregnation method is chosen, the ceria must be nanoscale (<7 nm) and oxygen defect-rich to enable nucleation and stronger binding of the copper oxide clusters and create type B sites. The resulting catalyst has good activity and stability for low-temperature WGS reactions.

Acknowledgements

The financial support of this work by the DOE/BES-Hydrogen Fuel Initiative program (#DE-FG02-05ER15730), the MRSEC Program of the NSF (#DMR-0213574), and New York State Office of Science, Technology and Academic Research (NYSTAR) is gratefully acknowledged. Research was carried out in part at the Center for Functional Nanomaterials, Brookhaven National Laboratory, which is supported by the U.S. Department of Energy, under Contract Number DE-AC02-98CH10886.

References

[1] D.S. Newsome, Catal. Rev. Sci. Eng. 21 (1980) 275.
[2] C. Rhodes, G.J. Hutchings, A.M. Ward, Catal. Today 23 (1995) 43.
[3] M. Mavrikakis, A.A. Gokhale, J.A. Dumesic, J. Am. Chem. Soc. 130 (2008) 1402.
[4] J.L.G. Fierro, J. Soria, J. Sanz, J.M. Rojo, J. Solid State Chem. 66 (1987) 154.
[5] C. Padeste, N.W. Cant, D.L. Trimm, Catal. Lett. 18 (1993) 305.
[6] T. Bunluesin, R.J. Gorte, J.G.W. Graham, Appl. Catal. B 15 (1998) 107.
[7] Y. Li, Q. Fu, M. Flytzani-Stephanopoulos, Appl. Catal. B 27 (2000) 179.
[8] Q. Fu, A. Weber, M. Flytzani-Stephanopoulos, Catal. Lett. 77 (2001) 87.
[9] Q. Fu, H. Saltsburg, M. Flytzani-Stephanopoulos, Science 301 (2003) 935.
[10] X. Qi, M. Flytzani-Stephanopoulos, Ind. Eng. Chem. Res. 43 (2004) 3055.
[11] W. Ruettinger, X. Liu, R. Farrauto, US Patent 20020141938.
[12] W. Ruettinger, X. Liu, R.J. Farrauto, Appl. Catal. B 65 (2006) 135.
[13] W. Deng, M. Flytzani-Stephanopoulos, Angew. Chem. Int. Ed. 45 (2006) 2285.
[14] X. Wang, J.A. Rodriguez, J.C. Hanson, D. Gamarra, M. Fernández-García, A. Martínez-Arias, J. Phys. Chem. B 109 (2005) 19595.
[15] X. Wang, J.A. Rodriguez, J.C. Hanson, D. Gamarra, A. Martínez-Arias, M. Fernández-García, J. Phys. Chem. B 110 (2006) 428.
[16] N.A. Koryabkina, A.A. Phatak, W.F. Ruettinger, R.J. Farrauto, F.H. Ribeiro, J. Catal. 217 (2003) 233.

[17] P. Djinović, J. Batista, A. Pintar, Appl. Catal. A 347 (2008) 23.
[18] F. Zhang, S.-W. Chan, J.E. Spanier, E. Apak, Q. Jin, R.D. Robinson, I.P. Herman, Appl. Phys. Lett. 80 (2002) 127.
[19] R. Si, M. Flytzani-Stephanopoulos, Angew. Chem. Int. Ed. 47 (2008) 2884.
[20] J.I. Langford, J. Appl. Crystallogr. 4 (1971) 259.
[21] J.I. Langford, J. Appl. Crystallogr. 6 (1973) 190.
[22] A. Guinier, Theorie et Technique de la Radiocristallographie, 3rd edition, Dunod, Paris, 1964, p. 482.
[23] T.H. Dekeijser, J.I. Langford, E.J. Mittemeijer, A.B.P. Vogels, J. Appl. Crystallogr. 15 (1982) 308.
[24] W. Liu, M. Flytzani-Stephanopoulos, J. Catal. 153 (1995) 304;
W. Liu, M. Flytzani-Stephanopoulos, J. Catal. 153 (1995) 317.
[25] K. Zhi, Q. Liu, R. Zhao, R. He, L. Zhang, J. Rare Earths 26 (2008) 538.
[26] X.-D. Zhou, W. Huebner, Appl. Phys. Lett. 79 (2001) 3512.
[27] F. Zhang, P. Wang, J. Koberstein, S. Khalid, S.-W. Chan, Surf. Sci. 563 (2004) 74.
[28] C. Zerva, C.J. Philippopoulos, Appl. Catal. B 67 (2006) 105.
[29] D. Gamarra, G. Munuera, A.B. Hungría, M. Fernández-García, J.C. Conesa, P.A. Midgley, X.Q. Wang, J.C. Hanson, J.A. Rodríguez, A. Martínez-Arias, J. Phys. Chem. C 111 (2007) 11026.
[30] S. Pengpanich, V. Meeyoo, T. Rirksomboon, K. Bunyakiat, Appl. Catal. A: Gen. 234 (2002) 221.
[31] N. Hedley, H. Tabachnik, Chemistry of Cyanidation, American Cyanamid Company, Wayne, NJ, 1968.
[32] L. Kundakovic, M. Flytzani-Stephanopoulos, Appl. Catal. A 171 (1998) 13.
[33] X. Tang, B. Zhang, Y. Li, Y. Xu, Q. Xin, W. Shen, Appl. Catal. A 190 (2000) 25.
[34] C. Lamonier, A. Ponchel, A. D'Huysser, L. Jalowiecki-Duhamel, Catal. Today 50 (1999) 247.
[35] L. Kundakovic, M. Flytzani-Stephanopoulos, J. Catal. 179 (1998) 203.
[36] W. Liu, M. Flytzani-Stephanopoulos, Chem. Eng. J. 64 (1996) 283.
[37] P. Zimmer, A. Tschöpe, R. Birringer, J. Catal. 205 (2002) 339.
[38] S. Tanuma, C.J. Powell, D.R. Penn, Surf. Interface Anal. 21 (1994) 165.
[39] H. Kušar, S. Hočevar, J. Levec, Appl. Catal. B 63 (2006) 194.
[40] M. Nolan, S.C. Parker, G.W. Watson, Surf. Sci. 595 (2005) 223.
[41] A. Pintar, J. Batista, S. Hočevar, J. Colloid Interface Sci. 307 (2007) 145.
[42] X. Zhang, K.J. Klabunde, Inorg. Chem. 31 (1992) 1706.
[43] L. Li, Y. Zhan, Q. Zheng, Y. Zheng, X. Lin, D. Li, J. Zhu, Catal. Lett. 118 (2007) 91.
[44] L. Barrio, M. Estrella, G. Zhou, W. Wen, J.C. Hanson, A.B. Hungría, A. Hornés, M. Fernández-García, A. Martínez-Arias, J.A. Rodríguez, J. Phys. Chem. C 114 (2010) 3580.
[45] A.S. Quiney, Y. Schuurman, Chem. Eng. Sci. 62 (2007) 5026.
[46] L. Li, Y.Y. Zhan, Q. Zheng, Y.H. Zheng, C.Q. Chen, Y.S. She, X.Y. Lin, K. Wei, Catal. Lett. 130 (2009) 532.